Multiple helical scans and the reconstruction of over FOV-sized objects in cone-beam CT*

Han Yu(韩 玉)[a], Yan Bin(闫 镔)[a)†], Li Lei(李 磊)[a],
Yu Chao-Qun(宇超群)[b], Li Jian-Xin(李建新)[a], and Bao Shang-Lian(包尚联)[c]

[a] *Information Engineering Institute, Information Engineering University, Zhengzhou* 450002, *China*
[b] *Surveying & Mapping Institute, Information Engineering University, Zhengzhou* 450002, *China*
[c] *Beijing City Key Laboratory of Medical Physics & Engineering, Peking University, Beijing* 100871, *China*

(Received 22 October 2011; revised manuscript received 21 February 2012)

In cone-beam computed tomography (CBCT), there are often cases where the size of the specimen is larger than the field of view (FOV) (referred to as over FOV-sized (OFS)). To acquire the complete projection data for OFS objects, some scan modes have been developed for long objects and short but over-wide objects. However, these modes still cannot meet the requirements for both longitudinally long and transversely wide objects. In this paper, we propose a multiple helical scan mode and a corresponding reconstruction algorithm for both longitudinally long and transversely wide objects. The simulation results show that our model can deal with the problem and that the results are acceptable, while the OFS object is twice as long compared with the FOV in the same latitude.

Keywords: large object, multiple helical scans, reconstruction algorithm, cone-beam computed tomography

PACS: 87.59.–e, 07.85.–m **DOI:** 10.1088/1674-1056/21/6/068701

1. Introduction

Because of the extra speed and high space resolution, cone-beam computed tomography (CBCT) has been widely used in industrial non-destructive testing. In CBCT, the projection data are typically collected in a circular source trajectory on the condition that the object is completely covered by the field of view (FOV). But when the object is over FOV-sized (OFS), the projection data is truncated, which causes the conventional filtered-back-projection (FBP)-type algorithm[1] to be invalid. In recent years, region-of-interest (ROI) reconstruction algorithms[2−4] and incomplete-data reconstruction algorithms[5,6] have been so well developed that ROIs can be reconstructed from truncated projection data. However, what we want to reconstruct is not a part of the large object but the whole large object. In this case, the ROI and incomplete-data reconstruction algorithms (e.g. the multiple scanning then splicing method) are not very suitable due to their poor efficiencies. In order to solve the problem, other scan modes have been developed, such as the helical scan mode for long object,[7,8] the bias-scan,[9−11] the half-scan,[12] and the rotation-translation (RT)[13,14] scan mode for short objects with a long transverse radius, as shown in Fig. 1(a). All of these scan modes are for either long or short objects with a long transverse radius, but they are invalid for long objects with a long transverse radius, as shown in Fig. 1(b).

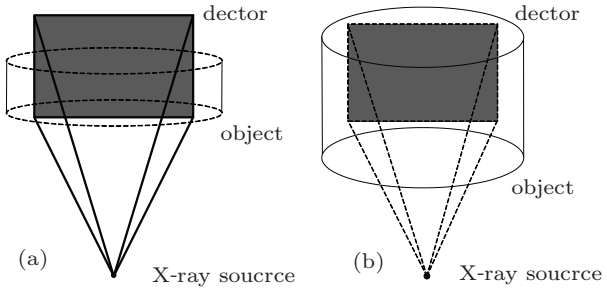


Fig. 1. Schematic diagram showing the objects to be tested. (a) A short object with a long transverse radius, and (b) a long object with a long transverse radius.

To examine the long object with a long transverse radius, we propose a multiple helical scan mode and corresponding reconstruction algorithm which can en-

*Project supported by the National Basic Research Program of China (Grant No. 2011CB707701), the National High Technology Research and Development Program of China (Grant No. 2009AA012200), and the National Nature Science Foundation of China (Grant No. 30970722).

†Corresponding author. E-mail: ybspace@yahoo.com.cn

© 2012 Chinese Physical Society and IOP Publishing Ltd

large the FOV length of the CBCT more than twice in the same latitude. The method is briefly described as follows. In the scanning step, multiple helical scans can be performed by translating the turntable, and consequently multiple sets of helical projection data are acquired. Referring to Ref. [15], we deduce the reconstruction algorithm based on the geometry of multiple helical scans. When reconstructing, first we rebin the multiple sets of projection data into one set of oblique parallel projection data which cover the whole object in the transverse direction. Then, the FBP-type algorithm is implemented to obtain the reconstruction result. For simplicity, the derivation for our formula is limited to the triple helical scan mode, which can be easily extended to the general multiple helical scan mode.

2. Multiple helical scan mode and its virtual equivalence

In this section, the multiple helical scan mode and its virtual equivalence are introduced. For simplicity, we introduce only the triple helical scan mode here.

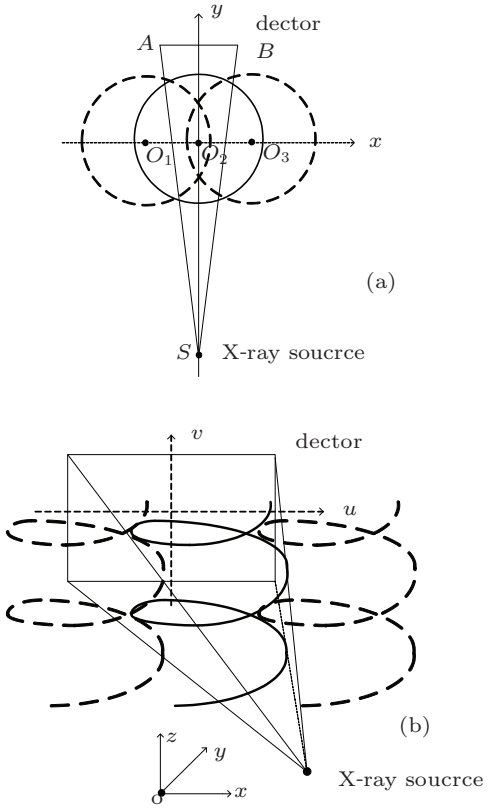


Fig. 2. The triple helical scan mode, (a) top view and (b) side view.

As shown in Fig. 2, S denotes the X-ray focus, the line segment AB represents the flat panel detector which is on the u–v plane, the sector area between the line segments SA and SB approximately denote the FOV of CBCT, and the circles centred at O_1, O_2, and O_3 denote triple helical tracks of the turntable when scanning. The coordinates system $oxyz$ is arranged as follows: O is the origin located at O_2; and the x axis and y axis are, respectively, vertical and parallel to the flat panel detector AB. In the triple helical scan mode, the X-ray source and the flat panel detector are fixed and the centre of the turntable can be translated to positions O_1, O_2, and O_3, respectively. The three sets of projection data corresponding, respectively, to O_1, O_2, and O_3 are obtained from three helical rotations which have the same helical pitch, collection interval, number of collections, and original altitude.

For the convenience of the derivation in Section 3, a virtual scan mode is introduced, which is equivalent to the multiple helical scan mode. It is obvious that the translation of the turntable along the x axis corresponding to a stationary X-ray source and flat panel detector is equivalent to a synchronous translation of the X-ray source and the flat panel detector along the opposite direction of the x axis corresponding to a fixed turntable, and a helical rotation of the turntable around O in a clockwise direction is equivalent to a synchronous rotation of the X-ray source and the flat panel detector

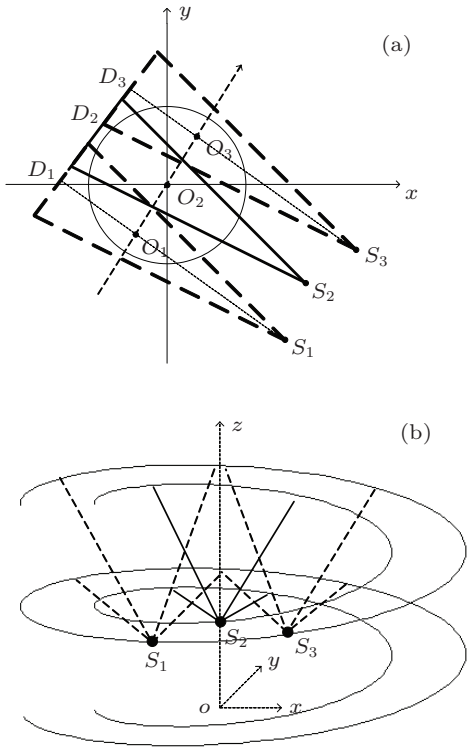


Fig. 3. A virtual scan mode equivalent to the triple helical scan mode, (a) top view, (b) side view.

around O in an anti-clockwise direction. Therefore, the triple helical scan mode shown in Fig. 2 is equivalent to the virtual scan mode shown in Fig. 3, where the X-ray focus S_2 of the middle cone-beam is located on the helical track with the center O_2 and the radius r_2=$r = |S_2O_2|$, and the X-ray focuses S_1, S_3 of the two-side cone-beams are both located on the helical track with the centre O_2 and the radius r_1= r_3=$\sqrt{r^2+|O_2O_1|^2}$, here let $|O_2O_1| = |O_2O_3|$.

3. Image reconstruction algorithm for the multiple helical scan mode

The proposed algorithm for the multiple helical scan mode contains three steps: rebinning, filtering, and back-projection.

3.1. Rebinning

Three truncated projection data sets $(i,\ \beta,\ v,\ u)$ are acquired via triple helical scans, where $i = 1, 2, 3$, β is the projection angle, and (v, u) denotes the pixel on the flat panel detector. In order to resolve the transverse data truncation, data rebinning is adopted first. Referring to Ref. [15], we only use the projection data within the Tam window[16,17] and rebin the data from three data sets $(i,\ \beta,\ v,\ u)$, $i = 1, 2, 3$, to one larger set $(\alpha,\ s,\ t)$ consisting of oblique parallel beams which are parallel when seen from above, where α is the projection angle after rebinning and (s, t) denotes the pixel on the virtual detector after rebinning, as shown in Fig. 4. Although the oblique parallel beams come from different positions of the X-ray source and have different cone angles, they shape a perfectly rectangular window of height $h/2$ on the t–s plane, which can be called the virtual rectangular detector after rebinning, and is shown in Fig. 4, where h is the helical pitch.

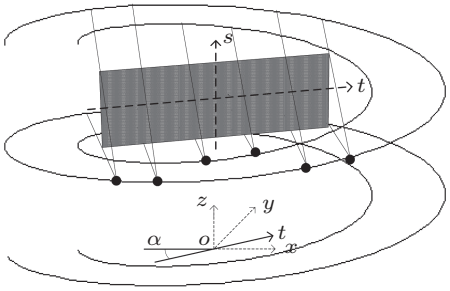


Fig. 4. Beam geometry after parallel rebinning.

Suppose that the first helical scan has the maximal distance t_1 between the X-ray and the rotation centre O_2, and the third helical scan has the minimal distance t_3, so in the new data set (α, s, t), the data with t less than t_1 comes from the data set $(1, \beta, v, u)$, the data with t more than t_3 comes from the data set $(3, \beta, v, u)$, and the rest comes from the data set $(2, \beta, v, u)$. This can not only ensure data integrality but also avoid superposition during rebinning.

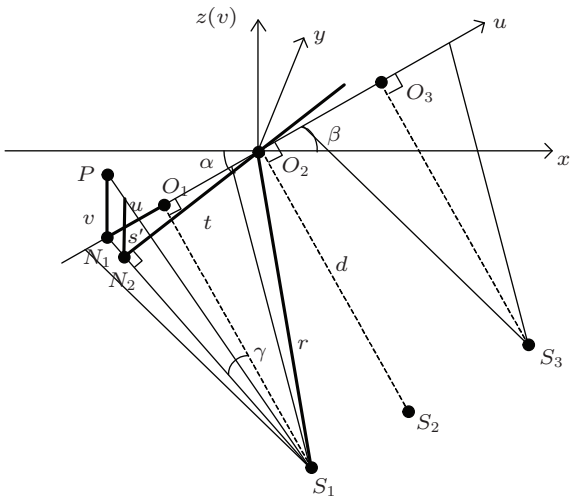


Fig. 5. Beam geometry of rebinning.

From Fig. 5, it can be seen that

$$\beta = \alpha - \gamma, \tag{1}$$

$$u = d \times \tan\gamma, \tag{2}$$

$$\frac{v}{s'} = \frac{S_1N_1}{S_1N_2}, \quad S_1N_2 = \sqrt{r^2+t^2},$$

$$S_1N_1 = S_1N_2 + t \times \tan\gamma. \tag{3}$$

Then we have

$$v = \frac{\sqrt{r^2+t^2} + t \times \tan\gamma}{\sqrt{r^2+t^2}} \times s'. \tag{4}$$

Let (t_0, s_0) denote the centre of the virtual rectangular detector after rebinning, t_0 the position where the t axis and the rotation axis cross, and s_0 the intersection of the rotation axis and the central ray in the oblique parallel beams. So the s of one X-ray is relative to the X-ray source position of the central ray in the oblique parallel beams, and during rebinning the s' which is relative to the X-ray source position where the X-ray source emits the X-ray, as seen in Fig. 6, must be figured out.

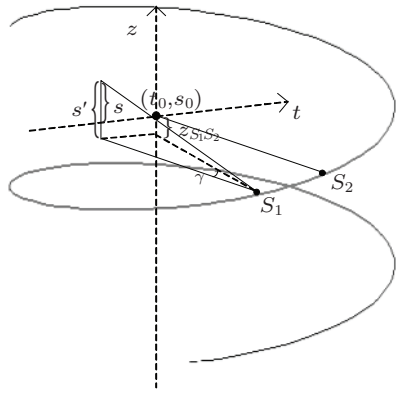


Fig. 6. Schematic for s' and s.

As shown in Fig. 6, $s' = s + z_{s_1s_2}$ and $z_{s_1s_2} = z_{s_1} - z_{s_2}$, where $z_{s_1s_2}$ denotes the altitude difference between S_1 and S_2 when the X-ray source turns γ degrees, and $z_{s_1s_2} = (h \times \gamma)/360$, so $s' = s + (h \times \gamma)/360$. Substitute s' into Eq. (4), then the result will be

$$v = \frac{\sqrt{r^2+t^2} + t \times \tan\gamma}{\sqrt{R^2+t^2}} \times (s + \frac{h \times \gamma}{360}). \quad (5)$$

By the geometry, it can be concluded that

$$\Delta o_1 = |o_1o_2|; \quad \Delta o_2 = 0; \quad \Delta o_3 = |o_3o_2|;$$
$$r_i = \sqrt{d^2 + \Delta o_i^2}, \quad i = 1,2,3;$$

so,

(i) $t \le t_1$, $\gamma = \arccos(\Delta o_1/r_1) - \arccos(t/r_1)$;

(ii) $t_1 < t < t_2$, $\gamma = \arccos(t/r_2)$;

(iii) $t \ge t_2$, $\gamma = \arccos(t/r_3) - \arccos(\Delta o_3/r_3)$.

Therefore, the rebinning process can be described as

$$p_{\rm re}(\alpha,t,v) = p\Big(i, \alpha-\gamma, d\times\tan\gamma, \frac{\sqrt{r^2+t^2}+t\times\tan\gamma}{\sqrt{r^2+t^2}} \times (s+\frac{h\times\gamma}{360})\Big), \quad (6)$$

where

i) $t \le t_1$, $i = 1$, $\gamma = \arccos(\Delta o_1/r_1) - \arccos(t/r_1)$;

ii) $t_1 < t < t_2$, $i = 2$, $\gamma = \arccos(t/r_2)$;

iii) $t \ge t_2$, $i = 3$, $\gamma = \arccos(t/r_3) - \arccos(\Delta o_3/r_3)$.

3.2. Filtering

The algorithm has fast and simple filtering by applying the one-dimensional ramp filter to each detector row separately before back-projection. After preweighting with the cosine of the cone angle, the filtering acts as a standard ramp-filtering, which produces

$$P_{\rm f}(\alpha,t,s) = (p_{\rm re}(\alpha,t,s) \times \cos(k(t,s))) \times g(t), \quad (7)$$

where $k(t,s)$ is the angle between the ray and the plane xy, and $g(t)$ is the ramp-filter.

3.3. Back-projection

The height of the virtual rectangular detector is $h/2$ after rebinning, which is half the pitch. Assume that there is a point (x,y,z), through which passes a ray that hits the upper edge of the virtual detector. As the source and detector move upwards, the projection of the point will move downwards on the detector surface. After half a turn, because of symmetry, the bottom edge of the virtual detector passes through the point (x,y,z), so it can be concluded that any point in the rearranged reconstruction space is illuminated for exactly half a turn, which means that the back-projection only needs data within 180°. The back-projection formula is

$$f(x,y,z) = \frac{1}{\pi}\int_{\theta(x,y,z)-\pi/2}^{\theta(x,y,z)+\pi/2} P_f(\alpha, t(x,y,\alpha), s(x,y,z,\alpha))\,{\rm d}\alpha, \quad (8)$$

where, $\theta(x,y,z) = (z - z_0) \times 2\pi/h$, z_0 is the initial height of the X-ray source when rotating, h is the helical pitch, and $t(x,y,\alpha)$ and $s(x,y,z,\alpha)$ denote the positions on the virtual rectangular detector where the point (x,y,z) is projected.

4. Data integrity and transverse expansion rate

In order to make sure of the integrity of the projection data, the object must be completely covered by a cone beam in the transverse direction during multiple helical scans. As figure 7 shows, it must be met that $t_{1\,\max} > t_{2\,\min}$, $t_{2\,\max} > t_{3\,\min}$, and $|t_{1\,\min} + t_{3\,\max}|$ is bigger than the maximal length of the scanned object in the transverse direction.

The rate of transverse expansion is the ratio between the transverse radius of multiple helical scans and that of a single helical scan. As shown in Fig. 7, the rate is $\frac{\min(|t_{1\,\min}|,|t_{3\,\max}|)}{\min(|t_{2\,\min}|,|t_{2\,\max}|)}$.

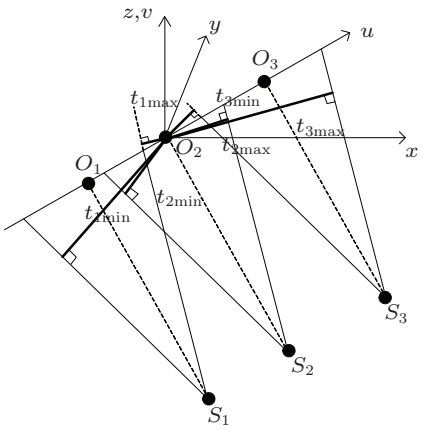


Fig. 7. Schematic diagram for analysing the data integrity and the rate of transverse expansion.

5. Numerical simulations

In this section, numerical simulations are conducted to validate and evaluate the proposed algorithm for the multiple helical scan mode compared with the helical Feldkamp–Davis–Kress (FDK)[18] for the standard helical scan mode.[19] A three-dimensional (3D) Shepp–Logan phantom is used to evaluate the reconstruction algorithms, and the experimental parameters are shown in Table 1.

As shown in Table 1, in the multiple helical scan mode, a detector with a pixel matrix 256×200 is used, while the pixel matrix of the detector for the standard helical mode is 256×512. Projection data obtained by the two data acquisition modes are reconstructed by the proposed algorithm for multiple helical scans and the helical FDK for the standard helical scan mode, respectively. The reconstructed results are shown in Figs. 8(a) and 8(c). In Figs. 8(b) and 8(d), the image profiles along the 256th row of the image in Figs. 8(a) and 8(c) are displayed with solid curves, respectively. The corresponding true profile in the original phantom is plotted with the dotted curve.

Table 1. The numerical simulation parameters.

Parameters	Triple helical scan mode	Standard helical scan mode
The distance between the focus and the origin/mm	300	300
The distance between the focus and the detector/mm	900	900
Pixel matrix of Shepp-Logan phantom	$512 \times 512 \times 512$	$512 \times 512 \times 512$
Pixel pitch of Shepp-Logan phantom/mm	0.0493	0.0493
Pixel matrix of the detector/pixels	256×200	256×512
Pixel pitch of detector/mm	0.148	0.148
Δo_1, translational distance of 1st helical scan/mm	-174×0.0493	
Δo_2, translational distance of 2nd helical scan/mm	0	
Δo_3, translational distance of 3rd helical scan/mm	174×0.0493	
Pitch/mm	200×0.0493	200×0.0493
The number of projections in each circle	360	360
Pixel pitch of reconstruction/mm	0.0493	0.0493
Matrix of reconstruction	$512 \times 512 \times 512$	$512 \times 512 \times 512$
Rate of transverse expansion	2.73	0
Rate of longitudinal expansion	2	2

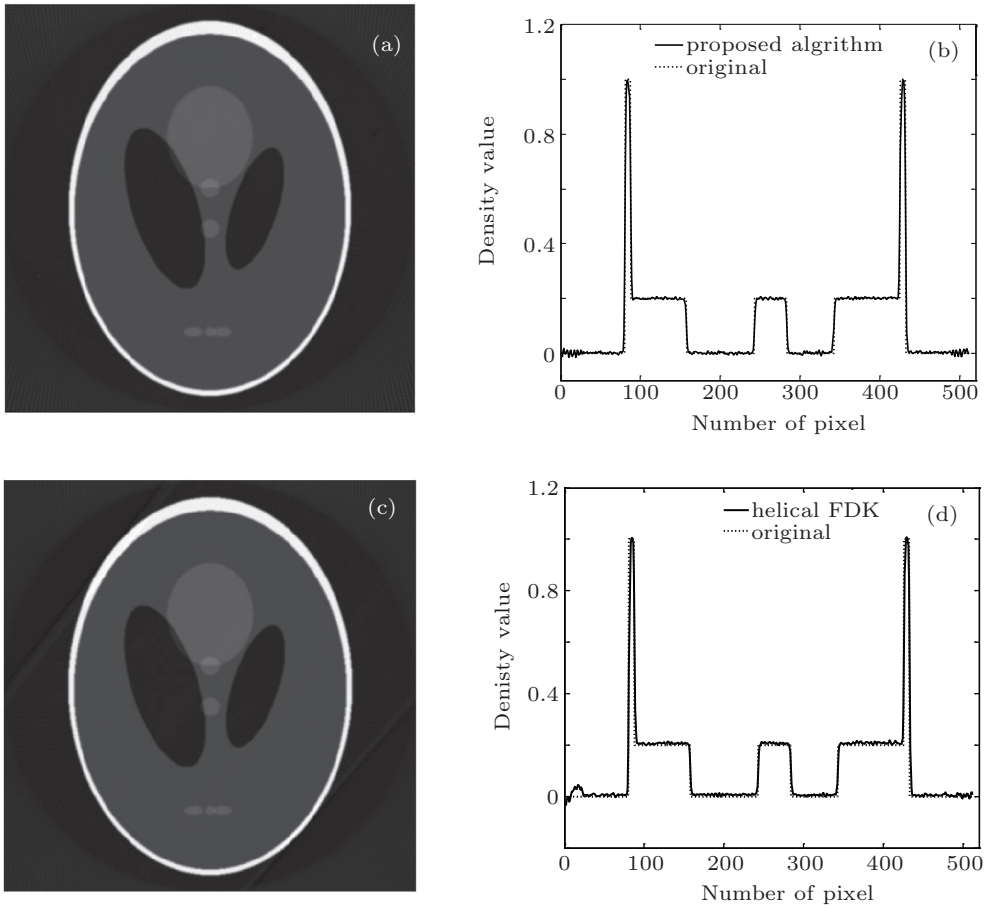


Fig. 8. Reconstructed images of the Shepp–Logan phantom at $z = 0$ mm, by (a) the proposed algorithm for the triple helical scan mode, and (c) the helical FDK for the standard helical scan mode, respectively. Panels (b) and (d) show the corresponding profiles along the 256th row of the images.

To further evaluate the reconstruction algorithms, the root of mean square errors (RMSEs) for the images reconstructed by two algorithms are computed using Eq. (9), and the results are shown in Table 2.

$$\mathrm{RMSE} = \sqrt{\frac{1}{N}\sum_{i=1}^{N}(f_{\mathrm{phantom}} - f_{\mathrm{reconstruction}})^2}. \quad (9)$$

Table 2. RMSEs for the reconstructions in Figs. 8(a) and 8(c).

Methods	RMSE
Proposed algorithm for multiple helical scan mode	0.0019
Helical FDK for the standard helical scan	0.0042

The results of simulation experiments show that the proposed algorithm for the triple helical scan mode is available, and even this method realizes two times the longitudinal expansion and 2.73 times the transverse radius expansion of the FOV. By comparison, it can be seen that the reconstruction image of the proposed algorithm for the triple helical scan mode is superior to that of the helical FDK for the standard helical scan mode. This is because rebinning has turned the three sets of truncated projection data into one set of non-truncated projection data, so there is no transverse truncated artifact in the reconstruction for the triple helical scan mode, the same as the reconstruction for the standard helical scan mode. The proposed algorithm only requires the data in the Tam window, which can reduce the artifact caused by larger cone angle projections.

6. Conclusions

Unavoidably, large objects need to be tested, so a multiple helical scan mode and its corresponding reconstruction algorithm for some CBCT cases are proposed. The main point of this method is to deal with the problem of OFS object size, and it performs a successful test for long objects with long transverse radii. In addition, the extended rate of the FOV length can

be more than twice in the same latitude. The simulation results show that the entire oversized phantom can be reconstructed in an acceptable way by the proposed algorithm. All these advantages have shown that the method used in this paper is meaningful for testing OFS objects in CBCT.

References

[1] Feldkamp A L, Davis L C and Kress J W 1984 *Opt. Soc. Am.* A **1** 612

[2] Zou Y, Pan X C and Sidky E Y 2005 *Opt. Soc. Am.* **22** 2372

[3] Yu L, Xia D, Zou Y, Pan X C, Pelizzari and Munro P 2006 *IEEE Trans. Med. Image.* **25** 869

[4] Li L, Kang K J, Chen Z Q, Zhang L and Xing Y X 2009 *J. X-ray Sci. Tech.* **17** 135

[5] Sidky E Y and Pan X C 2008 *Phys. Med. Biol.* **53** 4777

[6] Wang L Y, Li L, Yan B, Jiang C S, Wang H Y and Bao S L 2010 *Chin. Phys.* B **19** 088106

[7] Wang G, Lin T H, Cheng P C, Shinozaki D M and Kim H 1991 *Proc. SPIE* **1556** 99

[8] Kudo H and Satio T 1991 *Nuclear Science Symposium and Medical Imaging Conference* November 2–9, 1991 Baldwin, Santa Fe, USA, p. 1958

[9] Wang G 2002 *Med. Phys.* **29** 1634

[10] Li L, Chen Z Q, Zhang L, Xing Y X and Kang K J 2006 *High Energy Phys. Nucl. Phys.* **30** 812 (in Chinese)

[11] Fu J and Gong L 2006 *Opt. Tech.* **32** 209 (in Chinese)

[12] Fu J and Lu H N 2005 *Journal of Beijing University of Aeronautics and Astronautics* **31** 966 (in Chinese)

[13] Gong L, Fu J, Lu H N and Zhao F 2006 *Opt. Tech.* **32** 567 (in Chinese)

[14] Chen M, Zhang H T and Zhang P 2008 *Progress in Natural Science* **18** 209

[15] Turbell H and Danielsson P E 1999 *Proc. IEEE Medical Imaging*, November 8–14, 1998 Toronto, Canada, p. 1424

[16] Tam K C 1995 *US Patent* **2** 5390112

[17] Danielsson P E, Edholm P and Seger M 1997 *International Meeting on Fully Three-Dimensional Image Reconstruction in Radiology and Nuclear Medicine* Pennsylvania, June 25–28, 1997 USA, p. 141

[18] Wang G, Lin T H, Cheng P C and Shinozaki D M 1993 *IEEE Transactions on Medical Imaging* **12** 486

[19] Wang G, Ye Y B and Yu H Y 2007 *Phys. Med. Biol.* **52** R1